A real-time TEM study of the deformation mechanisms in β-Ti reinforced bulk metallic glass composites

Author links open overlay panel Lin Tian [a b], R. Lakshmi Narayan [c], Kun Zhou [d], Rita Babicheva [d], Upadrasta Ramamurty [d e], Zhi-wei Shan [a]

[a] Center for Advancing Materials Performance from the Nanoscale (CAMP-Nano), Hysitron Applied Research Center in China (HARCC), State Key Laboratory for Mechanical Behavior of Materials, Xi'an Jiaotong University, Xi'an, Shaanxi, 710049, PR China
[b] Institute of Materials Physics, University of Göttingen, Niedersachsen, 37077, Germany
[c] Department of Materials Science and Engineering, Indian Institute of Technology, Delhi, Hauz Khas, New Delhi, 110016, India
[d] School of Mechanical & Aerospace Engineering, Nanyang Technological University, 50 Nanyang Avenue, 639798, Singapore
[e] Institute of Materials Research and Engineering, Agency for Science, Technology and Research (A ∗STAR), Singapore 138634, Republic of Singapore

Abstract

The deformation mechanisms in a β-Ti reinforced Zr-based bulk metallic glass composite (BMGC) are studied by extracting submicron sized tensile coupons of the crystalline and amorphous phase in their monolithic and bilaminate composite forms and tensile testing them inside a TEM. Results show that the monolithic BCC crystalline phase and amorphous phase have high yield strains, owing to small length scale effects, but undergo negligible post-yield elongation before failure. However, the ductility of the bilaminate composite is significantly higher (~12.4%), provided the thickness of its amorphous portion is < 100 nm. Real time videos, which are supplemented by molecular dynamics simulations, show that the negligible post yield elongation of the monolithic BCC crystalline phase is caused by planar slip on one of the {110} planes. However, the bilaminate composite form exhibits strain hardening, despite the occurrence of planar slip, as dislocations pile up at the impervious amorphous/crystalline interface, which in turn, activates slip on other {110} planes. Strain hardening in the crystalline phase ceases when a shear band nucleated in the amorphous phase penetrates the dendrite along one of the slip planes. These mechanisms are extended to explain the flow behavior of β-Ti reinforced BMGCs and strategies to improve the ductility are discussed.

Keywords

In situ mechanical testing; Dislocations; Plasticity; Composite; Amorphous alloys; bcc crystals

1. Introduction

Bulk metallic glasses (BMGs) exhibit extraordinary strength and resilience but suffer from poor ductility in uniaxial tension when tested at temperatures well below their glass transition temperatures, T_g [1]. This is because plasticity in them manifests in the form of shear bands, which, in the absence of a microstructure, propagate unhindered and lead to failure without the homogenization of plasticity [2,3]. One widely accepted strategy to impart ductility to BMGs is to adopt a composite approach, which involves the incorporation of crystalline phases within the amorphous matrix, with the expectation that such reinforcements will interact with the shear bands and prevent their unmitigated propagation [[4], [5], [6], [7], [8], [9]]. Amongst different types of BMG matrix composites (BMGCs), the ones where a crystalline β-Ti phase is precipitated in the amorphous matrix in the dendritic form, during solidification from the melt, are considered most desirable as they exhibit the best combination of mechanical properties [4,5]. One important drawback of these BMGCs is that although they exhibit significant elongation to failure, they possess lower strengths compared to monolithic BMGs. This relatively lower strength of the BMGC is attributed to the presence of the softer β-Ti phase within the hard amorphous matrix [10,11].

It has been shown that the mechanical properties, such as strength and elongation to failure, of these BMGCs can be optimized to a reasonable degree by adjusting microstructural parameters such as the size, morphology, spacing, and volume fraction of the β-Ti phase [[12], [13], [14]]. Alternately, some recent studies have shown that simultaneous and significant improvement in strength and ductility can be achieved by introducing transformation induced plasticity (TRIP) in the β-Ti phase [[15], [16], [17], [18], [19], [20]]. From these studies, a comprehensive set of correlations between microstructural parameters and the mechanical properties were developed. For instance, it was broadly recognized that increasing the size and volume fraction of dendrites enhanced the elongation to failure [12,19,21]. In contrast, increasing the interdendritic spacing has a deleterious effect on the elongation to failure. While molecular dynamics (MD) simulations [22,23] and finite element (FEM) simulations [[24], [25], [26], [27]] have been employed to understand the deformation mechanisms in the dendrites and interactions of shear bands with them, direct experimental observations remain elusive.

In this study, we address this particular aspect by extracting submicron sized tensile specimens of the crystalline dendritic phase and amorphous phase--in their

monolithic and bilaminate composite forms--from a β-Ti reinforced BMGC and perform in situ tensile tests inside a transmission electron microscope (TEM) to observe their deformation mechanisms. The experimental observations are utilized to rationalize the tensile stress-strain response of the bulk BMGC specimen. We believe that this study will not only provide explanations for the microstructure-mechanical property correlations in these BMGCs but also help in designing BMGCs that exhibit enhanced ductility and toughness.

2. Experiments

An arc-melted BMGC with the nominal composition $Zr_{36.6}Ti_{31.4}Nb_7Cu_{5.9}Be_{19.1}$ was used in this study. This alloy, also referred to as DH1 [[5], [52],12], is heated above its liquidus temperature (~2000 K) and then slowly cooled on a water cooled copper plate at a cooling rate of 100 K/s. A cube with dimensions of 3 mm × 3 mm × 3 mm (length × breadth × thickness) is extracted from the ingot and cloth-polished (with 0.25 μm diamond paste) to a mirror finish for microstructural investigations in a scanning electron microscope (SEM). In the representative micrograph of the composite displayed in Fig. 1a, several dendrites with lighter contrast embedded within a matrix that has a darker contrast can be seen. Energy dispersive spectroscopy reveals that the dendritic phase and matrix phase have compositions of $Zr_{37.9}Ti_{47.2}Cu_{1.5}Nb_{13.4}$ and $Zr_{33.9}Ti_{26}Cu_{9.1}Nb_{3.5}Be_{27.5}$, respectively. X-ray diffraction scans (see Refs. [5,12] for more details) indicate that the dendritic phase has body centered cubic (BCC) crystal structure while the matrix is amorphous [12]. Specimens for the macro-scale tensile testing were prepared from an ingot of DH1 as per the ASTM E8M standard [28]. The nominal diameter of the gauge section was 1.5 mm and the gauge length was 10 mm. Two specimens of the alloy were tested at room temperature in a screw-driven universal testing machine. The tests were performed with a constant cross-head displacement rate of 1 μm/s. The cross-head displacement was utilized to estimate strains as the tensile specimens were too small to accommodate an extensometer.

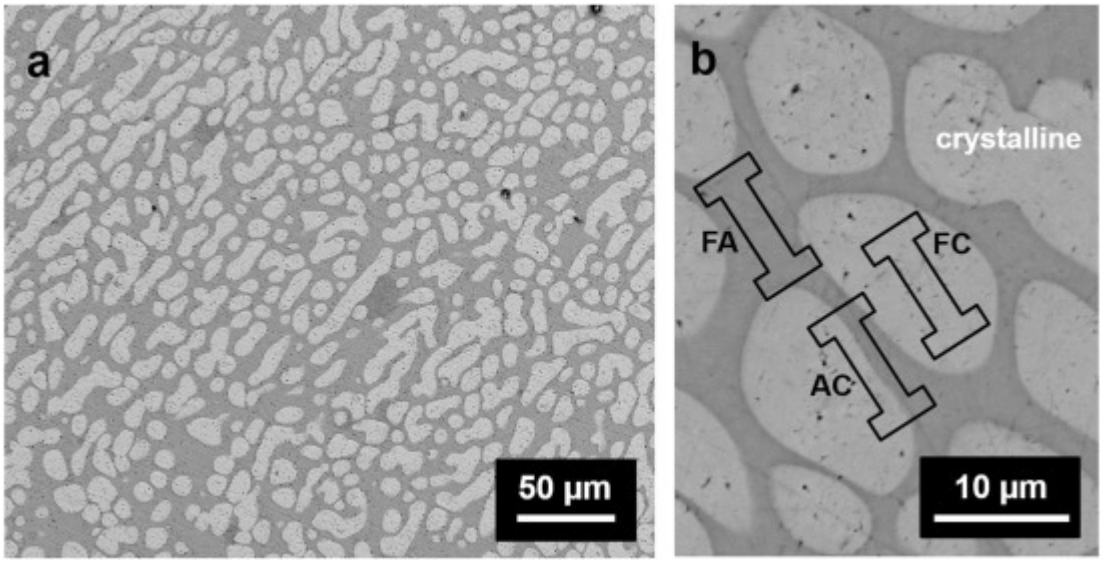

1. Download: Download high-res image (794KB)
2. Download: Download full-size image

Fig. 1. (a) Representative microstructure of the β-Ti dendrite reinforced bulk metallic glass matrix composite (BMGC). (b) High magnification image on which schematic illustrations of the three different types of the in-situ tensile specimens that were extracted and tested: fully amorphous (FA), fully crystalline (FC), and amorphous/crystalline (AC).

The in-situ tensile specimens were prepared in the following manner. A 1 μm thick film of this BMGC is placed in a dual beam focused ion beam/scanning electron microscope (FIB/SEM) (FEI Nanolab 600). This film was further thinned to 800 nm using FIB. Since free-standing tensile specimens undergo shaking at load, $P < 50$ μN, and are not suitable for performing simultaneous high resolution imaging, an alternate push-to-pull fixture is designed using FIB on the BMGC film [29]. Further information on this fixture is provided elsewhere [30]. I-shaped specimens with approximate lengths of 1000–1200 nm, widths of ~380–600 nm and a thickness of 80 nm are fabricated at the center of this fixture. The specimen is attached to 2 μm wide struts and the entire assembly is supported in the base by a single 2 μm wide strut. When the two upright struts are loaded, they move apart and generate a uniaxial tensile strain in the I-shaped specimen [30]. I-shaped tensile specimens were extracted from three representative regions marked on the micrograph shown in Fig. 1b. Specimens extracted from fully crystalline and fully amorphous regions are labelled as FC and FA, respectively. The two specimens extracted from region containing both amorphous and crystalline phases are referred to as AC-1 and AC-2. To minimize ion beam-induced damage, the final FIB trim of the I-specimens was carried out using mild milling conditions of 16 kV and ~10 pA. Note that the relatively higher thickness of the convex pillars in the push-to-pull fixture ensures that they do not deform permanently until the I-shaped tensile specimen fails. This is confirmed by the near elastic recovery of the pillars on unloading. Moreover, the higher thickness of the pillars dampens the vibrations induced by the loading tip and stabilizes the testing setup. Additionally, rectangular compression specimens, with dimensions 700 nm × 400 nm × 80 nm (length × breadth × thickness), are also extracted from regions A and B (see Fig. S1a and S1b in Supplementary Information (SI) for the images). Both tensile and compression tests were performed inside a transmission electron microscope (TEM, JEOL 2100 F) with a Hysitron PicoIndenter 95 (PI95) holder and the entire test was recorded in real time. For the push-to-pull fixtures, the loading rate was set as 1–5 nm/s, which corresponds to a strain rate of 4×10^{-3} s^{-1} in the I-shaped specimen. The compression tests on the rectangular specimens were conducted at a strain rate of 2×10^{-3} s^{-1}. Videos of all tests were recorded using a charge-coupled device camera (Gatan 833 CCD) (inside the TEM) that has the maximum capture rate of 10 frames/s. The uniaxial tensile strain in the I-shaped specimens was measured from analyzing frames from the recorded in situ TEM videos of the test in ImageJ. Details of the measurement procedure are provided in Refs. [31,32].

3. Molecular dynamics simulations

The absence of reliable interatomic potentials for a Zr–Ti–Nb–Cu–Be based crystalline alloy led us to choose Ti-45at%V system as the model material. Vanadium stabilizes the BCC structure of Ti at room temperature. Hence, the alloy is representative to the β-Ti dendrites of the BMGC employed in this study [33,34]. Molecular dynamics (MD) simulation was conducted for a computational cell in the form of a rectangular parallelepiped with dimensions, 80 × 120 × 325 $Å^3$. Then two different models were developed in the study, namely, a monolithic crystalline laminate and an amorphous/crystalline bilaminate. The visualizations of these models are shown in Fig. 2a and b, respectively. To develop the monolithic crystalline model, a cell with 200,000 Ti atoms is created. This cell has a bcc structure in the initial state. Then, 45% of Ti atoms in this model were randomly replaced by V atoms to obtain the desired composition. The amorphous phase in the amorphous/crystalline bilaminate model was obtained by first melting the Ti–V cell, which is followed by quenching it to the room temperature. Note that the amorphous-crystal interface in the bilaminate model was parallel to the *x*-*z* plane and the crystallographic orientations of the monolithic crystalline and amorphous/crystalline models were chosen to mimic the orientations of the FC and AC-1 specimens, respectively (see section 2). Henceforth, they will be referred to as FC_{model} and AC_{model}.

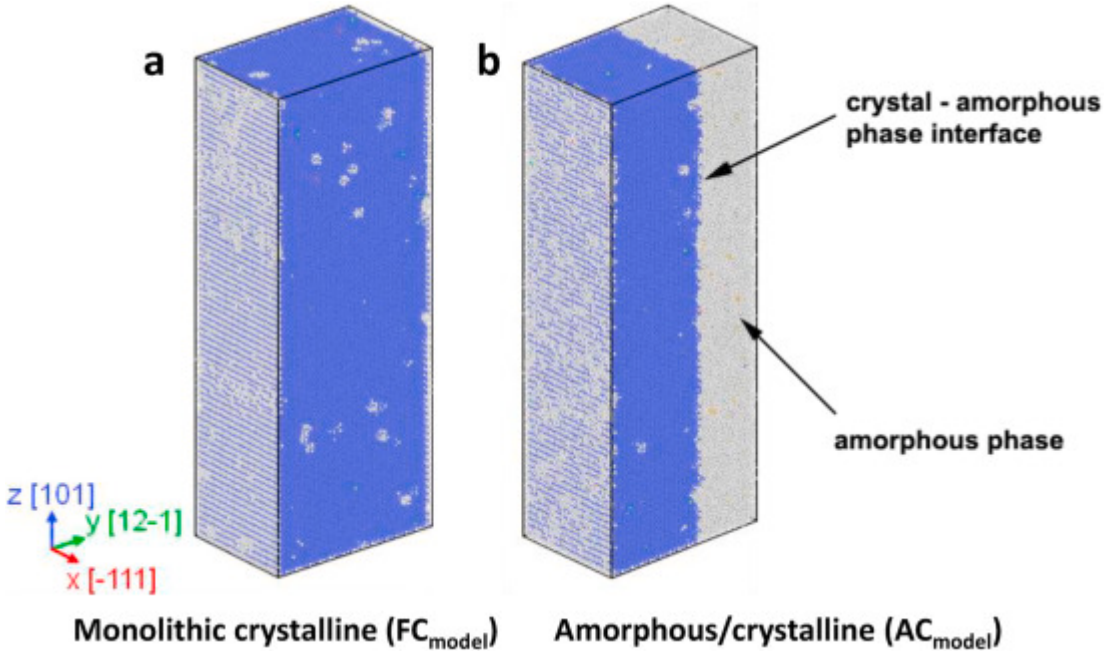

1. Download: Download high-res image (602KB)
2. Download: Download full-size image

Fig. 2. Three-dimensional view of (a) the Ti-45at.%V monolithic crystalline (FCmodel) and (b) the amorphous/crystalline (ACmodel) model samples that were studied using the molecular dynamics simulations. These samples are produced after energy minimization and equilibration at room temperature (300 K). Blue color represents the bcc crystal lattice whereas the grey color represents the amorphous alloy. (For

interpretation of the references to color in this figure legend, the reader is referred to the Web version of this article.)

MD simulation was performed using the atomic/molecular massively parallel simulator (LAMMPS) program package [35]. Atomic interactions in the Ti-45at.%V alloy were described by the modified embedded-atom method (MEAM) interatomic potential developed by Maisel et al. [33]. Before deformation, the materials were relaxed at zero temperature to obtain the state of the minimum potential energy. Then, the models were equilibrated for 20 ps at 300 K in the NPT (constant number of atoms, pressure and temperature) ensemble keeping normal stress components along the x, y and z axes equal to zero.

During further uniaxial tensile deformation (up to 20%) at 300 K in the NPT ensemble, the periodic boundary conditions along the *x* and *z* axes, and free boundaries in the *y*-direction were set. The tensile deformation was applied along the *z*-axis with the strain rate of 10^{8} s^{-1}. OVITO software was used for visualization of the atomic structure and dislocation analysis was performed using the dislocation extraction algorithm (DXA) [36].

4. Results

4.1. Microstructure and tensile behavior of bulk DH1 composite

The volume fraction of dendrites, V_d, interdendritic spacing, λ, and dendrite size, δ, are estimated (from micrographs such as those displayed in Fig. 1a) as 51%, 3.7 ± 2.1 μm and 11.5 ± 7.5 μm, respectively. A representative stress, σ, vs. strain, ε, plot of the DH1 composite is shown in Fig. 3. After yielding (yield strength, σ_y ~1000 MPa), it undergoes work hardening and has an ultimate tensile strength, UTS ~1160 MPa. Note that the specimen undergoes uniform elongation of only ~1% beyond yield although the total strain to failure, ε_f ~4%. This is due to the fact that after the initial work hardening stage, macroscopic localization of flow (or necking) occurs; thereafter, the flow stress drops gradually until failure.

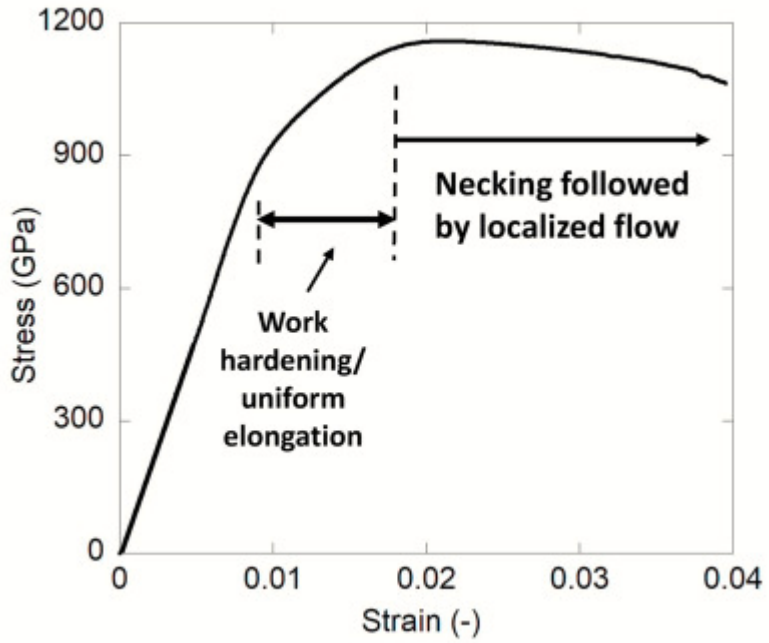

1. Download: Download high-res image (251KB)
2. Download: Download full-size image

Fig. 3. Representative tensile stress–strain response measured on a bulk specimen of the DH1 composite.

4.2. In situ tensile behavior of FA, FC and AC specimens

To understand the individual and collective deformation responses of the crystalline and amorphous phases in DH1, the tensile tests on the FC, FA and AC submicron sized specimens were conducted. A bright field image of the undeformed FC specimen and its selected area diffraction (SAED) pattern are shown in Fig. 4a. The FC specimen is

a single crystal BCC β-Ti phase, which has a width and length of 400 nm and 1000 nm, respectively. While imaging of the specimen is performed along [$\bar{1}$11] zone axis, tensile strain is applied along [101] crystallographic direction. This particular orientation was chosen on the basis that it is one of the dominant orientations of the dendrites in as cast DH1 [37]. Successive bright field TEM snapshots from the video recording (see Video S1 in supplementary information (SI)) of the tensile test are shown in Fig. 4a–d. The FC specimen undergoes uniform elongation to ε ~2.2% following which, a small dark feature appears at the top-left corner of it (see Fig. 4c). This feature is tentatively assumed to be a signature of dislocations and its formation is an indication that yielding has initiated. (The reason behind this assumption will be provided later.) One drawback of using the push-to-pull device is that the variations in σ during the deformation of the specimen could not be recorded. However, compression tests on the FC phase are conducted to obtain σ_y which is 987 ± 30 MPa (see Fig. S1c in SI). While this matches well with the strength determined from micropillar compression studies on this phase [11], its bulk counterpart has a much lower σ_y of 600 MPa and yield strain, ε_y, of ~0.2% [38]. The comparatively higher σ_y and ε_y (~2.2%) of the FC specimen is attributed to dislocation starvation and dislocation source truncation effects observed in miniaturized crystalline materials [39]. While the first mechanism suggests that the decrease in the dimensions of the specimen makes it difficult to operate dislocation sources, the latter states that the overall content of dislocation sources reduces in smaller volumes of the material [39]. Regardless of the operative mechanism, activation of dislocation slip, to accommodate plasticity, requires higher stresses and strains in submicron crystals.

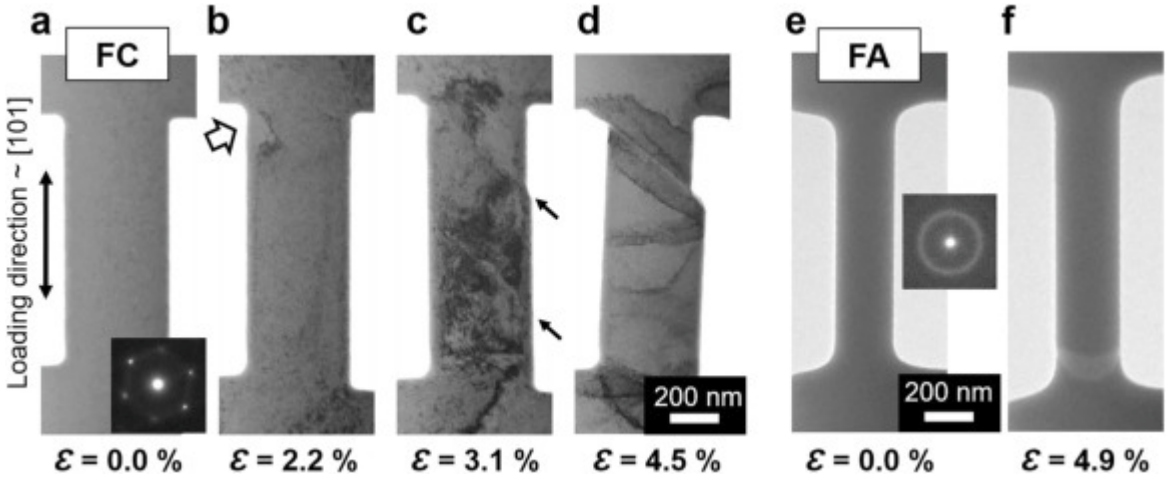

1. Download: Download high-res image (347KB)
2. Download: Download full-size image

Fig. 4. (a) Bright field TEM image and SAED pattern (inset) of the fully crystalline (FC) specimen before the tensile test. (b–d) TEM images extracted from the real time recording of the test at strains, ε of (b) 2.2%, (c) 3.1%, and (d) 4.5%. (e–f) Bright field TEM images of FA specimen (e) prior to testing and (f) at ε of ~4.9%.

With a further increase in ε, more dislocations nucleate in the FC specimen. When ε ~3.1%, a thin slip band, which extends from the top-left corner of the specimen and propagates at an angle, θ ~45° to the loading axis, was noted. It creates a surface offset (see Fig. 4c) on the right edge of the specimen. About 400 nm away from this offset, another parallel slip band forms simultaneously in the middle of the specimen. Beyond ε ~3.1%, the specimen fails via the rapid growth of the surface offset and does not undergo further uniform elongation (see Fig. 4d). Analysis of the SAED pattern reveals that the slip band forms along the $(1\bar{1}0)$ plane, which is one of the primary slip planes in BCC crystals.

The bright field TEM image of the undeformed, 380 nm wide FA specimen is displayed in Fig. 4e and its corresponding SAED pattern in included in the inset. Concentric rings in the SAED pattern confirm that the FA specimen is fully amorphous. On applying load, it undergoes uniform elongation and fails abruptly after yielding at ε ~4.9%, as shown in Fig. 4f (see also Video S2). A similar ε_y was reported by Tian et al. [31] in similar sized monolithic amorphous tensile specimens. The σ_y of the amorphous phase, determined from compression tests, is 2300 ± 60 MPa (see Fig. S1c). In contrast, the σ_y and ε_y of the bulk amorphous phase (BMGs) are 2000 MPa and 2%, respectively [1]. The much higher ε_y of the submicron sized FA specimen, compared to that of its bulk counterpart, is also attributed to a defect starvation effect which is analogous to that observed in crystalline materials. In small volumes of the amorphous phase, the number of shear transformation zones (STZs), which are the atomistic carriers of plasticity in them, is much lesser than that in a bulk BMG. Since a higher strain energy is required for nucleating more STZs, the former yields at higher σ and ε.

The AC-1 specimen, which is an amorphous/crystalline bi-laminate, is shown in dark field mode in Fig. 5a with the SAED patterns of the phases included as insets I and II, respectively. The narrower phase, which has a width of 90 nm, is amorphous as its SAED pattern consists of continuous rings (see inset I). The crystalline phase has a width of 380 nm and its SAED pattern (see inset II) is identical to that of the previously tested FC specimen (see Fig. 4a). Since the tensile axis is parallel to the amorphous/crystalline interface, both phases deform in the iso-strain condition when load is applied. Bright field TEM stills captured at different stages of the tensile test conducted on the AC-1 specimen are shown in Fig. 5b–f (see also Video S3). The specimen undergoes uniform elongation without any other perceptible changes until ε ~2.2%. Immediately thereafter, a diffuse band develops in the crystalline part of the specimen, which is marked with a white arrow in Fig. 5c and referred to as a 'type-A' band. This band, which is inclined at θ ~40° to the loading axis, originates from the bottom-left corner of the crystalline phase and terminates at the amorphous/crystalline interface. SAED pattern of the crystalline phase (inset II in Fig. 5a) reveals that the band is parallel to the $[1\bar{1}2]$ direction of the crystal. Surface offsets, if any, were not resolvable at either ends of this band and the specimen continues to undergo uniform elongation with increasing strain. At ε ~2.8%, four parallel,

equispaced thick dark bands, with a characteristic spacing of ~50 nm (marked with black arrows in Fig. 5c), appear at the bottom-left edge of the crystalline phase. Each of these, individually referred to as 'type-B' bands, extend along the [110] direction and terminate at the type-A band. Both the types of bands are also mutually perpendicular. When ε ~4.2%, another set of type-B and type-A bands form in the other half of the crystalline phase. Both these bands originate from the same location on the amorphous/crystalline interface and terminate at the left edge of the crystalline phase (marked with a white and black arrow in Fig. 5e). Meanwhile, at the free surface of the amorphous layer, which is close to the terminus of the previously formed type-A band, a surface offset develops (marked with a red arrow in Fig. 5e). This surface offset is colinear with the first type-A formed in the crystalline phase. However, unlike that seen in the FC specimen, the offset does not grow rapidly and lead to strain localization. Instead, the AC-1 specimen undergoes uniform elongation until ε ~12.4% and at intermediate values of ε, a few more type-B bands form within the crystalline phase (see Fig. S3a-b). However, at ε >12.4%, the shear offset widens and results in the formation of a crack. As the crack grows and penetrates the crystalline phase, all the bands disappear and only black patches that resemble dislocation debris remain in it (see Fig. S3c).

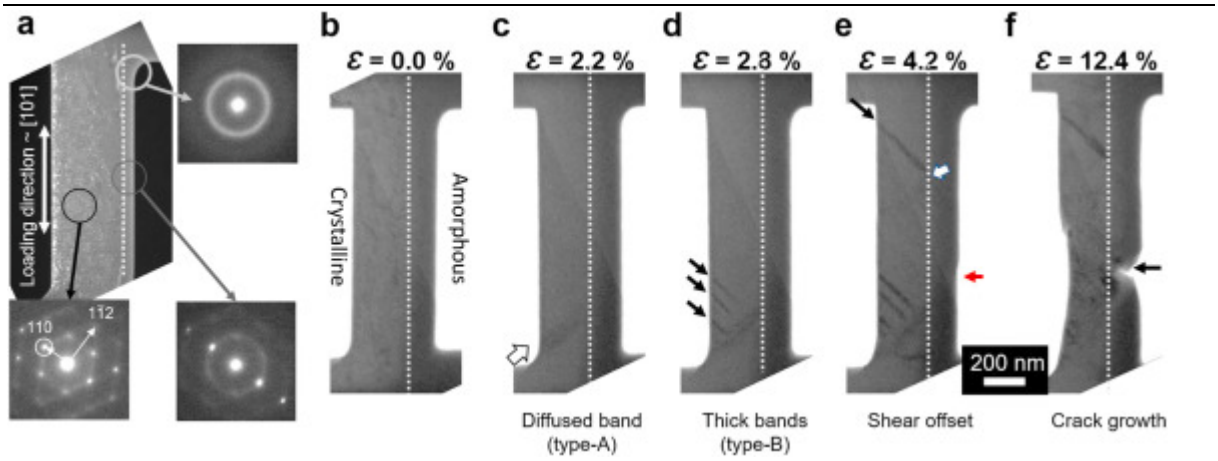

1. Download: Download high-res image (397KB)
2. Download: Download full-size image

Fig. 5. (a) Dark field TEM image of amorphous/crystalline specimen (AC-1) and the SAED patterns obtained on the two microstructural constituents. (b) Bright field TEM images extracted from the real time video recording of the test at ε of (b) 0%, (c) 2.2%, (d) 2.8%, (e) 4.2%, and (f) 12.4%.

Note that post-failure, the diffused and thick dark bands in AC-1 specimen disappeared, which meant that they could not be analyzed further. The tension test is repeated on the other amorphous/crystalline bi-laminate, AC-2 specimen, whose dark field TEM image is displayed in Fig. 6a. SAED patterns of the amorphous phase and crystalline phase are shown in insets I and II, respectively. The crystalline phase in AC-2 specimen is orientationally identical to the AC-1 specimen, i.e., their SAED patterns are the same, but the configurations and proportions of the two phases is different.

The AC-2 specimen consists of >50% of the amorphous phase and has a curved amorphous/crystalline interface, which is also not perfectly parallel to the loading axis. Due to this curvature, when AC-2 is tested in tension, it is likely that the phases in AC-2 specimen will not deform under iso-strain conditions. The curvature of the interface is an outcome of the curvature of the dendrites in the BMGC. Nevertheless, owing to the orientational similarity between the AC-1 and AC-2 specimen, the deformation mechanisms and the behavior of unit plasticity carriers in the two are also expected to be similar.

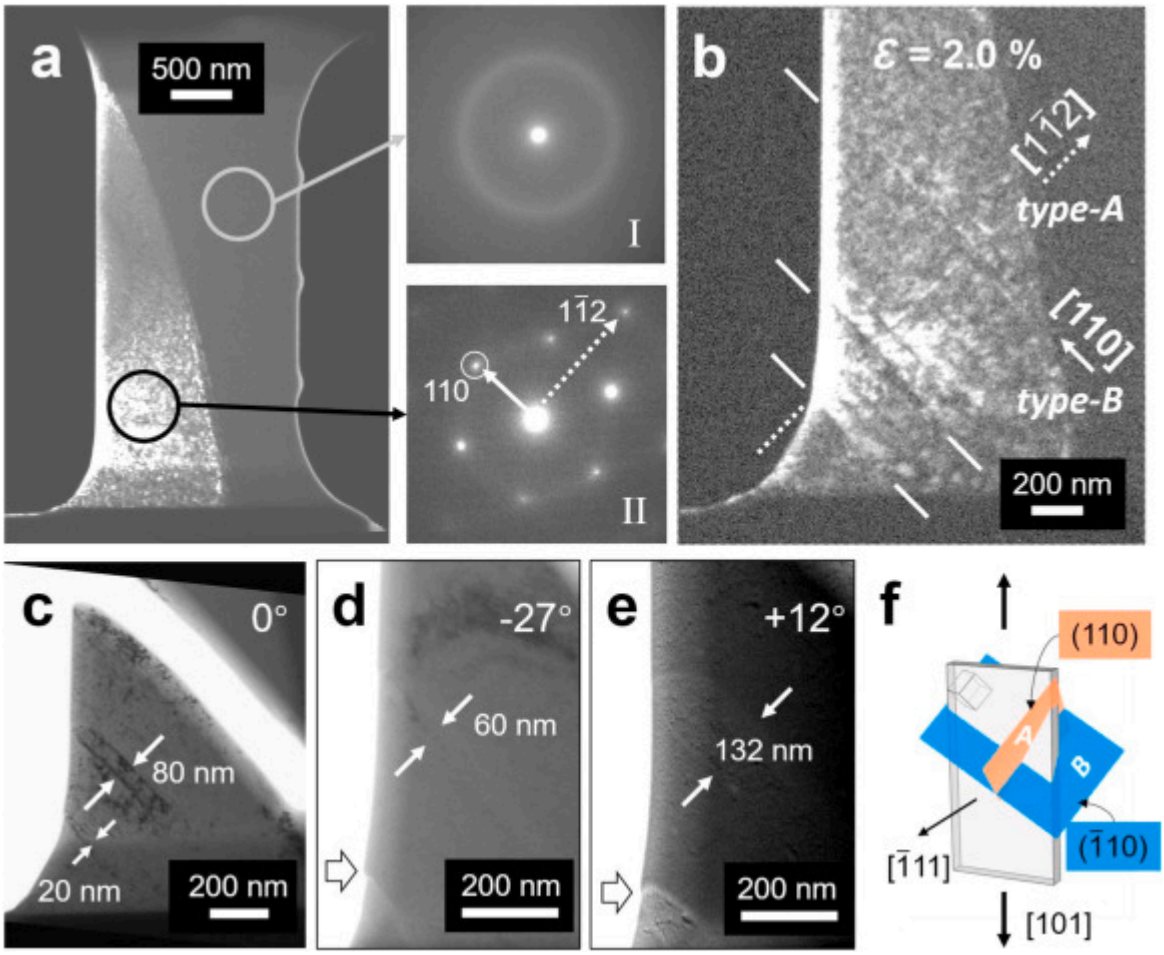

1. Download: Download high-res image (979KB)
2. Download: Download full-size image

Fig. 6. (a) Dark field TEM image of amorphous/crystalline specimen (AC-2). (b) SAED pattern of amorphous phase. (c) SAED pattern of crystalline phase. (d) Magnified dark field TEM image of AC-2 specimen at ε ~2%. (e) Bright field TEM image of the sample after failure and tilted at - 27°(f) and 12°(g). (h) A schematic of orientation of the bands in the sample.

The dark field TEM image of the AC-2 specimen after it is deformed to ε ~2% is shown in Fig. 6b. Much like what was seen in AC-1, type-A and type-B bands, form along the [110] and [1$\bar{1}$2] crystallographic directions of the crystalline phase in AC-2 specimen as well. Further straining of the AC-2 specimen to ε ~4% leads to the formation of a

macroscopic shear band in the amorphous phase. This shear band then propagates along one of the type-B bands in the crystalline phase and causes failure. Note that the ε_f of the AC-2 specimen is significantly lower than that of the AC-1 specimen. The bright field image of the failed portion of the crystalline phase is shown in Fig. 6c. Two of the type-B bands, with widths of 80 nm and 20 nm, remain preserved even after the failure of the specimen. To further observe the characteristics of these bands, the crystalline phase is imaged after tilting the specimen to angles, $\varphi \sim -27°$ and 12°, as shown in Fig. 6d and e, respectively. In both the tilted conditions, the widths of the bands change and they become lighter in contrast. At $\varphi \sim -27°$, a type-B band with thickness of 80 nm, reduces to 60 nm whereas at $\varphi \sim 12°$, it increases to 132 nm. A small surface offset is also visible at locations where type-A and type-B bands terminate at the edge of the crystalline phase (see white arrows in Fig. 6d and e).

From the above observations, the following inferences can be made regarding the band like features observed while testing AC-1 and AC-2 specimens. The type-A and type-B bands observed during deformation are slip traces in the crystalline phase of both the specimens. In BCC crystal, the dislocation with the $a/2$ <111> Burgers vector, where a is the lattice parameter of the crystalline phase, can glide on one of its (110), (112) or (123) planes [40]. From orientation analysis of the crystal, it appears that type-A and type-B bands are slip traces on two different (110) planes. Type-A bands are slip traces along the (110) plane, which intersects the $(1\bar{1}1)$ plane at 90°, along $[1\bar{1}2]$. In contrast, the type-B bands form along the $(1\bar{1}0)$ plane, which intersects $(1\bar{1}1)$ plane at 35.3° along $[1\bar{1}0]$. Note that differences in the thickness of type-A and type-B bands is the outcome of the relative inclinations between the slip planes and the $(1\bar{1}1)$ plane, which is also the viewing surface of the specimen. Since only the edge of the (110) plane intersects the viewing surface of the specimen, the dislocations on it hardly interacts with the electron beam. As a result, type-A bands produce minimal contrast during imaging and are often almost invisible (see Fig. 5c) or appear like a fine line (see Fig. 6b). In contrast, the oblique intersection of the $(1\bar{1}0)$ plane with the viewing surface exposes a significant portion of dislocations to the electron beam, which in turn results in type-B bands appearing thick (see Fig. 6e and Fig. S3a). The arrangement of these planes is illustrated in Fig. 6f and Fig. S3b. Therefore, the slip systems operating along type-B and type-A bands are $(1\bar{1}0)[111]$ and $(110)[1\bar{1}1]$, respectively.

4.3. Simulations of plastic deformation in FC and AC specimens

In Fig. 7a the simulation snapshots of FC_{model} and AC_{model} after $\varepsilon \sim 9\%$ tensile deformation are displayed. The atoms are color coded based on common neighbor analysis (CNA). Blue colored atoms are organized into the BCC crystal lattice, whereas the grey colored ones represent disordered regions, such as the amorphous phase, and regions with a high density of dislocations.

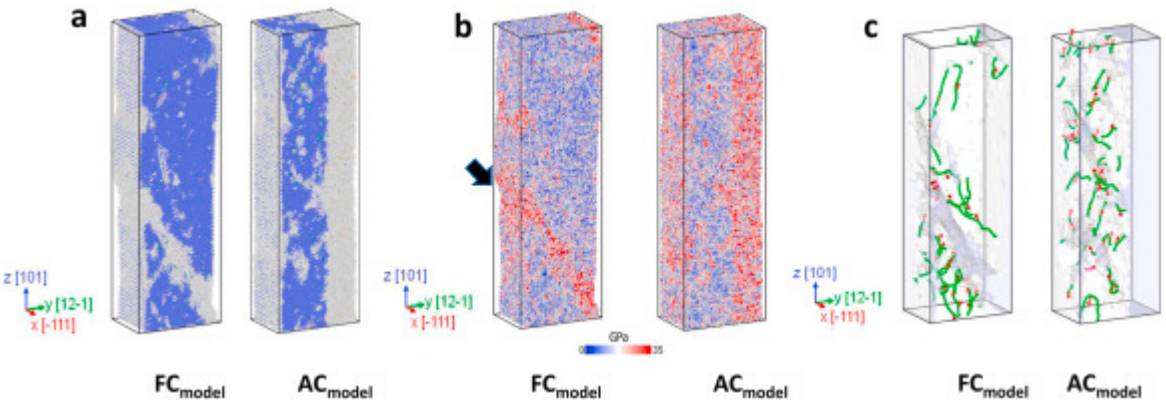

1. Download: Download high-res image (647KB)
2. Download: Download full-size image

Fig. 7. (a) Simulation snapshot of monolithic crystalline (FCmodel) and amorphous/crystalline (ACmodel) models at 9% tensile deformation, (b) the Von Mises equivalent stress distribution and (c) dislocation lines and defect mesh (in light-grey color), according to DXA, for the snapshot in (a). ½<111> dislocation lines are shaded in green and their Burgers vectors are indicated by red arrows. (For interpretation of the references to color in this figure legend, the reader is referred to the Web version of this article.)

The distribution of Von Mises equivalent stress in the two models are shown in Fig. 7b. From both images it is evident that stress concentrations develop along the [110] direction in FC_{model} (marked by black arrows in Fig. 7b), whereas it is relatively uniform in the crystalline part of AC_{model}. However, the atoms of the amorphous part are under higher stresses compared to those in the crystalline one in the latter.

Fig. 7c shows the dislocation structures formed in the two models. In both models, $a/2$ <111> dislocation segments are observed. However, in FC_{model}, slip only occurs on one of the $(1\bar{1}0)$ planes (see Fig. 7c). On further straining, shear localization occurs along one of these planes and leads to failure at ε_f ~10%. In contrast, slip gets simultaneously activated on several $(1\bar{1}0)$ and (110) slip planes in AC_{model}, which results in a more homogeneous distribution of dislocation segments in them. Also, the amorphous/crystalline interface does not allow the cross-over of dislocations to the amorphous phase leading to a pile up of dislocations on the slip planes. AC_{model} exhibits uniform elongation till ε ~17% and eventually fails by necking at ε ~20%. Overall, the dislocation slip behavior and the trend in variations of ε_f in the FC_{model} and AC_{model} are broadly similar to that observed in situ tensile tests conducted on FC and AC-1 specimens, respectively.

5. Discussion

In tension, DH1 undergoes plastic deformation in two stages. Strain hardening, which occurs in the first stage, occurs for significantly smaller ε than the second stage, where the BMGC undergoes strain softening. This asymmetry in the extent of the strain hardening and strain softening portion of the flow curve is also observed in several other β-Ti reinforced BMGCs [5,41]. To understand this aspect, the deformation mechanisms in the FA, FC and AC specimens will be first discussed and then the inferences from these will be taken as a reference to elucidate the deformation mechanisms in DH1 BMGC.

5.1. Deformation mechanisms in the FC and FA specimens

The uniform elongation in tension for the FC specimen with a BCC crystal structure and dimensions of 400–600 nm is only ε ~3.1%. In comparison, FCC single crystals of the same size [[42], [43], [44]], are significantly more ductile and often deform uniformly to ε ~30%. The lower ductility in the BCC crystals of the present study is an outcome of the occurrence of planar slip in them. In FCC crystals there are 12 equivalent slip systems on which dislocation slip is feasible. Simultaneous glide and cross slip of dislocations on different intersecting planes increases the interactions between them. The increased interactions between dislocations causes strain hardening, which necessitates the activation and glide of more dislocations at unstrained locations. This in turn, homogenizes plasticity in the FCC crystal and enhances its ductility. In contrast, although BCC crystals have 48 slip systems, none of the slip planes are close packed. Therefore, dislocation slip occurs only on one of its (110), (112) or (123) family of planes and the cross slip of dislocations to other planes is also limited. Our MD simulations also confirm that slip predominantly occurs only on one of the $(1\bar{1}0)$ slip planes in the monolithic crystalline model. This confinement of slip on a single plane is referred to as planar slip. Planar slip in submicron sized BCC crystals limits interactions between dislocations and allows them to exit the crystal without hindrance. The exit of multiple dislocations along this plane leads to the formation and growth of a surface offset on the crystal. Strain localization occurs along this surface offset which grows further and leads to failure, as was seen in the FC specimen (see Fig. 4d). This suggests that while dislocation slip occurs in the dendritic phase of the BMGC, it is not particularly ductile due to the occurrence of planar slip.

Similarly, the FA specimen also undergoes negligible plastic deformation after yielding, although its failure is more abrupt. This is because the mechanism of plastic deformation in the amorphous phase is significantly different from that in the crystalline phase. Macroscopic plasticity in BMGs manifests as shear bands, which in turn, form from the simultaneous activation of several STZs along the deformation plane. When BMGs are subjected to uniaxial tension, shear bands propagate unhindered, owing to the lack of an interacting ‘microstructure’, and cause abrupt

failure. However, there are two important stages of shear band formation, namely nucleation and maturation, which precede its propagation. While the nucleation of a shear band is conditional upon the availability of activable STZs, its maturation to a macroscopic shear band depends on a critical length, l ~20–100 nm, to which the nuclei can grow [45,46]. Therefore, even if a shear band nucleus forms successfully, it cannot propagate unless it attains this critical length. This becomes an important aspect in the deformation of submicron scale and nanoscale MGs as besides the lack of activable STZs in the material, the specimen dimensions approach this critical length scale. For instance, when the dimensions of the MG specimen approach 100 nm, a sharp rise in σ_y and a transition in the failure mechanism was observed [30,31]. Instead of deforming via the propagation of a mature shear band, the sample undergoes homogenous deformation followed by necking. However, since the FA specimen in this study is much wider (~350 nm), there is sufficient space for shear band nuclei to mature into macroscopic shear bands.

5.2. Deformation mechanisms in the AC-1 and AC-2 specimens

The amorphous/crystalline bi-laminate, AC-1 specimen, elongates uniformly till ε ~12.4%, which is significantly higher than linear combination of the failure ε of FA and FC specimens. A similar enhancement in ductility of Cu/CuZr crystalline-amorphous nanolaminates compared to its individual constituents has also been reported by earlier studies [47,48]. However, there are some crucial differences between these nanolaminates and the AC-1 specimen tested in the present study. First, the average width of the constituents in Cu/CuZr crystalline-amorphous nanolaminates is much lesser than 100 nm. In contrast, the width of the crystalline layer is > 100 nm and amorphous layer is ~90 nm in the AC-1 specimen. Second, as mentioned earlier, the interface in the Cu/CuZr crystalline-amorphous nanolaminates exhibit homogeneous deformation as the percolation of dislocations to the amorphous phase which in some cases, also results in the precipitation of nanocrystalline phases in the latter, relieves strains in the crystalline phase [49,50]. However, in the AC-1 specimen, there is no evidence to suggest that dislocations percolate to the amorphous phase nor was any phase transformation observed in it. It is then worth asking, what is the underlying mechanism that leads to high ductility of the AC-1 specimen?

We believe that the enhanced plasticity of the AC-1 specimen is the combined outcome of greater interactions between dislocations in the crystalline phase and the mitigation of shear band propagation in the amorphous phase. The mechanism for this is as follows. When the AC-1 specimen is loaded in tension, plasticity initiates in the crystalline phase by the activation of slip as it has a lower ε_y (~2.2%), whereas the amorphous phase continues deforming elastically. Since the Schmid factor for both $(1\bar{1}0)[111]$ and $(110)[1\bar{1}1]$ slip systems, loaded along [101], is ~0.408, both are equally likely to get activated. However, the choice of the operating slip system will be determined by additional factors such as local microstructural variations or some geometrical factor such as stress concentrations or local thermal fluctuations. For

instance, in the orientationally similar FC specimen (Fig. 4a–d), only the $(1\bar{1}0)[111]$ slip system (type A band) gets activated and since this leads to planar slip induced strain localization, the $(110)[1\bar{1}1]$ slip (type B band) does not even get activated. In the present set of experiments, it appears that the differences in stress concentrations from one of the corners of the I-shape tensile specimens could be the determining factor for the choice of the slip system. In the AC-1 specimen, the bottom-left corner is the point of initiation of slip along the (110) plane. However, unlike that seen in FC specimen, persistent slip along this plane in the crystalline phase of the AC-1 specimen does not lead to a surface offset on its other edge. This is because dislocations are unable to penetrate the amorphous/crystalline interface and cross over to the amorphous phase. As a result, dislocations pile up against the interface and start repelling the trailing dislocations, which in turn, leads to strain hardening along this plane. These dislocations are also confined to this plane owing to the low likelihood of cross slip in BCC crystals. Therefore, further straining will lead to activation of dislocation slip on other available slip planes. The operation of slip along $(1\bar{1}0)$ planes explains the formation of thick dark bands (type-A bands) adjacent to the diffused, low contrast band (type-B band) at ε ~2.8% in the crystalline phase (see Fig. 5c and d). When ε increases further, dislocations pile up along these planes as well, forcing the activation of other (110) and $(1\bar{1}0)$ slip planes in the crystalline phase (see Fig. 5e and Fig. S2a). At ε ~4.2%, yielding in the amorphous phase begins and a shear offset forms on free edge of the amorphous layer. However, this is not immediately followed by rapid propagation of a shear band as the width of the amorphous phase in the AC-1 specimen approaches the critical dimensions required for the maturation of a shear band nucleus. As a result, the deformation mechanism changes to homogeneous flow and the amorphous phase undergoes further uniform elongation. Eventually, the amorphous phase necks at ε ~12.4%, which leads to the formation of a crack, followed by the failure of the AC-1 specimen.

However, AC-2 specimen, which has a 250–500 nm wide amorphous phase, fails at a significantly lower ε despite the activation of slip on multiple slip planes of the crystalline phase. This is attributed to the formation of a mature shear band in the amorphous layer of the AC-2 specimen as it has a relatively larger width compared to that of the AC-1 specimen. Once this shear band matures, one of the activated $(1\bar{1}0)$ slip planes in the crystalline phase provides a channel for the shear band to propagate along it.

5.3. Flow behavior of the bulk DH1 BMGC in tension

On the basis of the above-described deformation mechanisms in the monolithic and bilayer composite specimens, the deformation mechanism of the DH1 tensile specimen is explained as follows. When the DH1 specimen yields, as mentioned earlier, plasticity initiates in the dendrites as they are relatively softer than the amorphous matrix [10]. Although planar slip occurs along either of $(1\bar{1}0)$ or (110) slip in the dendrite, dislocations pile-up at the amorphous/crystalline interface. This promotes

strain hardening and activates slip on other slip planes as was seen in AC-1 specimen. However, at ε ~2%, the amorphous phase yields and shear bands nucleate in the matrix. Since interdendritic spacing, λ is ~3.7 μm, there is sufficient space for the shear band to mature. When ε increases, the mature shear band penetrates the dendritic phase and propagates along one of its slip planes as was observed in both AC-1 and AC-2 specimens. The propagation of shear bands through the dendrite leads to the onset of strain softening of the DH1 BMGC specimen and facilitates strain localization and failure. This immediate onset of strain softening due to shear band nucleation at ε ~2% is the reason why the strain hardening portion of the flow curve is lower than that of the strain softening portion.

From this, it becomes evident that *the key to enhancing the extent of strain hardening and uniform elongation of BMGCs is to delay or mitigate shear band maturation and penetration within dendrites besides enhancing the interactions between dislocations within them*. Mitigation of shear band maturation--as seen in AC-1 specimen--can be ensured when $\lambda < 100$ nm, as there is insufficient width to form a mature shear band. One way to do this is to increase V_d and δ, at the expense of λ. This was indeed found to be true as DH3 alloys, whose V_d ~67–75%, are twice as ductile as DH1 alloys [12]. However, given that the dendritic phase is softer, increasing V_d beyond a certain value is also not feasible from a structural application point of view as it compromises the σ_y of the BMGC. *An alternate strategy to improve ductility without modifying V_d or λ and compromising on σ_y is to make the dendrite more resistant to shear band penetration*. We believe that this strategy is successfully implemented by the initiation of deformation induced martensitic transformations or TRIP in the β-Ti dendrites [15,18,19,51]. Martensitic transformation within the dendrite re-orients the slip planes and improves shear band arresting abilities of the dendrites in the following way. The reoriented slip planes cause more interactions between dislocations in the crystal which leads to greater strain hardening. Moreover, the transformed phase enhances the hardening rate further as its boundaries act as barriers for dislocation motion. Finally, owing to elevated levels of strain hardening within these reoriented planes of the dendrite, shear bands do not have access to a low resistance path for propagating through them. In fact, post-facto imaging of such BMGCs reveals that dendrites which undergo phase transformation to a martensitic phase are not penetrated by shear bands [[19], [53]]. As a consequence, these BMGCs resist shear localization in the form of necking and are significantly more ductile than BMGCs whose dendrites do not exhibit the TRIP effect. On the basis of this discussion, it can be concluded that ductility can be significantly enhanced by ensuring that the dendrites in the BMGC and have $\lambda < 100$ nm and they undergo martensitic transformation during deformation.

Before closing, it is worth questioning if extrapolating the deformation behavior of the submicron sized AC-1 and AC-2 specimens to explain the deformation mechanisms in bulk BMGC is an oversimplification on the following grounds. First, this study has only examined the interactions between a small portion of the dendrite and amorphous

phase. However, this may not necessarily be representative of deformation in the BMGC, which involves shear band interactions with multiple dendrites leading to the formation of dense shear band networks. Second, the interaction of a shear band with only one orientation of the dendrite has been considered in the study. However, the dendrites in the BMGC have several different orientations and it is unclear if other dendrites in the BMGC will offer a different degree of resistance to shear band penetration while undergoing strain hardening. Third, the study implicitly assumes that the defect content in the dendrites is low and that may lead to overestimation of the peak ductility and strength that can be realistically obtained in bulk specimens. However, in this context, a conscious effort was made to consider the length scale effects on deformation of submicron-sized specimens—as discussed in section 4.2—while extrapolating it to describe the deformation of bulk phases in the BMGC. Therefore, despite these concerns, we believe that this study offers reasonable insights to the deformation mechanisms in BMGCs and provides useful pointers that can help in designing stronger and tougher BMGCs.

6. Conclusions

With the aim of understanding the deformation mechanisms in a β-Ti reinforced BMGC in tension, submicron sized specimens of the BCC crystalline dendrite (FC), the amorphous matrix (FA) and a bilaminate composite of the two (AC-1 and AC-2) are extracted and tensile tested in real time inside a TEM. Results indicate that the FC and FA specimen, yield at large strains but exhibit negligible post-yield uniform elongation and fail due to shear localization via planar slip along a {110} plane and shear banding, respectively. In contrast, the crystalline phase of the co-axial amorphous/crystalline specimen undergoes significant strain hardening as the <111> dislocations in the dendrites pile-up against the impervious amorphous/crystalline interface, which activates slip on other {110} planes. MD simulations on a structurally similar amorphous/crystalline model further confirm this. Nevertheless, the ductility of these specimens depends on the onset of shear band maturation in the amorphous phase and its propagation through the crystalline phase, which in turn, depends on the thickness of the amorphous phase. On this basis, it was inferred that the transition from strain hardening to post-necking non-uniform elongation of the BMGC under tension can be extended to larger strains if (a) the thickness of the matrix is reduced below the critical limit required to nucleate a shear band or (b) the dendrite is rendered resistant to shear band penetration by some mechanism such as TRIP.

CRediT authorship contribution statement

Lin Tian: Experiments, Conceptualization, Methodology, Data curation, Writing – review & editingWriting reviewing and editing. **R. Lakshmi Narayan:** Experiments, Conceptualization, Methodology, Data curation, Writing – review & editingWriting reviewing and editing. **Zhou Kun:** Simulations, Writing – review & editingWriting reviewing and editing, Validation. **Rita Babicheva:** Simulations, Writing – review & editingWriting reviewing and editing. **Upadrasta Ramamurty:** Supervision, Writing – review & editingWriting reviewing and editing. **Zhi-wei Shan:** Supervision, Conceptualization, Writing – review & editingWriting reviewing and editing.

Declaration of competing interest

The authors declare that they have no known competing financial interests or personal relationships that could have appeared to influence the work reported in this paper.

Acknowledgements

Z.W.S acknowledges support from National Natural Science Foundation of China (51621063, and 5203000210), the National Key Research and Development

Program of China (No.2017YFB0702001). L.Tian acknowledges the Alexander von Humboldt Foundation, University of Göttingen, and the Start-Bridge-Finish Program from ICASEC for financial support. The authors thank Ms. Xin'ai Zhao for assistance in TEM experiment. RLN acknowledges the support of the Start-up research grant (SRG/2020/000095) from SERB, DST, GoI. The work at Nanyang Technological University was supported by the funding from A*STAR via the Structural Metals and Alloys Programme (No. A18B1b0061).

Appendix A. Supplementary data

Download all supplementary files included with this article
What's this?
The following are the Supplementary data to this article:

Media player

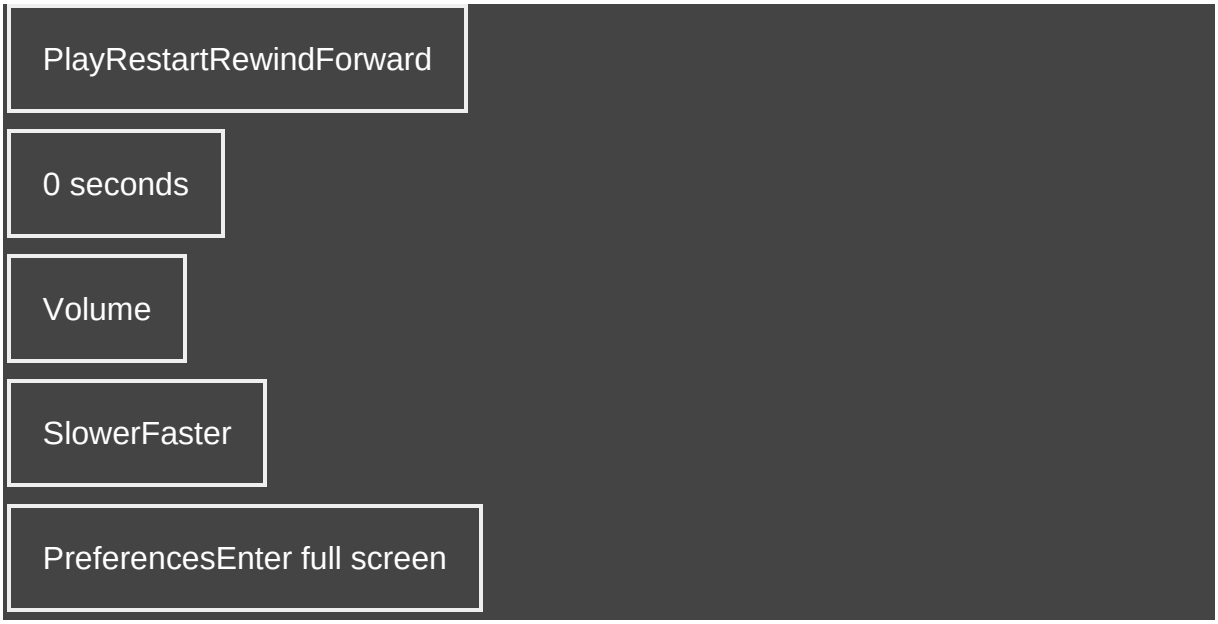

0:00 / 0:17Speed: 1x*Stopped*

Download: Download video (2MB)

Multimedia component 1.

Media player

PlayRestartRewindForward

Volume

SlowerFaster

PreferencesEnter full screen

0:00 / 0:14Speed: 1x*Stopped*

Download: Download video (1MB)

Multimedia component 2.

Media player

PlayRestartRewindForward

Volume

SlowerFaster

PreferencesEnter full screen

0:00 / 0:13Speed: 1x*Stopped*

Download: Download video (2MB)

Multimedia component 3.

Download: Download Word document (2MB)

Multimedia component 4.

References

[1]

C.A. Schuh, T.C. Hufnagel, U. Ramamurty

Mechanical behavior of amorphous alloys

Acta Mater., 55 (2007), pp. 4067-4109, 10.1016/j.actamat.2007.01.052
View PDFView articleView in ScopusGoogle Scholar

[2]

R. Narasimhan, P. Tandaiya, I. Singh, R.L. Narayan, U. Ramamurty

Fracture in metallic glasses: mechanics and mechanisms

Int. J. Fract. (2015), 10.1007/s10704-015-9995-3
View at publisherGoogle Scholar

[3]

K.B. Kim, J. Das, M.H. Lee, S. Yi, E. Fleury, Z.F. Zhang, W.H. Wang, J. Eckert

Propagation of shear bands in a Cu47.5Zr47.5Al5 bulk metallic glass

J. Mater. Res., 23 (2008), pp. 6-12, 10.1557/JMR.2008.0025
View in ScopusGoogle Scholar

[4]

D.C. Hofmann, J.-Y. Suh, A. Wiest, M.-
L. Lind, M.D. Demetriou, W.L. Johnson

Development of tough, low-density titanium-based bulk metallic glass matrix composites with tensile ductility

Proc. Natl. Acad. Sci. U.S.A., 105 (2008), pp. 20136-20140, 10.1073/pnas.0809000106
View in ScopusGoogle Scholar

[5]

D.C. Hofmann, J.-
Y. Suh, A. Wiest, G. Duan, M. Lind, M.D. Demetriou, W.L. Johnson

Designing metallic glass matrix composites with high toughness and tensile ductility

Nature, 451 (2008), pp. 1085-1089, 10.1038/nature06598
View in ScopusGoogle Scholar

[6]

S. Scudino, K.B. Surreddi, S. Sager, M. Sakaliyska, J.S. Kim, W. Löser , J. Eckert

Production and mechanical properties of metallic glass-reinforced Al-based metal matrix composites

J. Mater. Sci., 43 (2008), pp. 4518-4526, 10.1007/s10853-008-2647-5
View in ScopusGoogle Scholar

[7]

C. Fan, R.T. Ott, T.C. Hufnagel

Metallic glass matrix composite with precipitated ductile reinforcement

Appl. Phys. Lett., 81 (2002), p. 1020, 10.1063/1.1498864
View in ScopusGoogle Scholar

[8]

J. Eckert, J. Das, S. Pauly, C. Duhamel

Mechanical properties of bulk metallic glasses and composites

J. Mater. Res., 22 (2007), pp. 285-301, 10.1557/jmr.2007.0050
View in ScopusGoogle Scholar

[9]

D.C. Hofmann

Bulk metallic glasses and their composites: a brief history of diverging fields

J. Mater. (2013), 10.1155/2013/517904
2013
Google Scholar

[10]

R.L. Narayan, K. Boopathy, I. Sen, D.C. Hofmann, U. Ramamurty

On the hardness and elastic modulus of bulk metallic glass matrix composites

Scripta Mater. (2010), 10.1016/j.scriptamat.2010.06.010
Google Scholar

[11]

V. Hasannaeimi, S. Muskeri, B. Gwalani, D.C. Hofmann, S. Mukherjee

Deformation behavior of metallic glass composites and plasticity accommodation at microstructural length-scales

Mater. Today Commun., 24 (2020),
Article 101237, 10.1016/j.mtcomm.2020.101237
View PDFView articleView in ScopusGoogle Scholar
[12]

R.L. Narayan, P.S. Singh, D.C. Hofmann, N. Hutchinson, K.M. Flores, U. Ramamurty

On the microstructure–tensile property correlations in bulk metallic glass matrix composites with crystalline dendrites

Acta Mater., 60 (2012), pp. 5089-5100, 10.1016/j.actamat.2012.06.032
View PDFView articleView in ScopusGoogle Scholar

[13]

M. Calin, L.C. Zhang, J. Eckert

Tailoring of microstructure and mechanical properties of a Ti-based bulk metallic glass-forming alloy

Scripta Mater., 57 (2007), pp. 1101-1104, 10.1016/j.scriptamat.2007.08.018
View PDFView articleView in ScopusGoogle Scholar

[14]

J.L. Cheng, G. Chen, F. Xu, Y.L. Du, Y.S. Li, C.T. Liu

Correlation of the microstructure and mechanical properties of Zr-based in-situ bulk metallic glass matrix composites

Intermetallics, 18 (2010), pp. 2425-2430, 10.1016/j.intermet.2010.08.040
View PDFView articleView in ScopusGoogle Scholar

[15]

L. Zhang, Z. Zhu, H. Fu, H. Li, H. Zhang

Improving plasticity and work-hardening capability of β-type bulk metallic glass composites by destabilizing β phases

Mater. Sci. Eng., 689 (2017), pp. 404-410, 10.1016/J.MSEA.2017.02.070
View PDFView articleView in ScopusGoogle Scholar

[16]

Y. Wu, Y. Xiao, G. Chen, C.T. Liu, Z. Lu

Bulk metallic glass composites with transformation-mediated

work-hardening and ductility

Adv. Mater., 22 (2010), pp. 2770-2773

CrossrefView in ScopusGoogle Scholar

[17]

D. Liu, Z. Zhu, Z. Li, L. Zhang, H. Fu, A. Wang, H. Li, H.H. Zhang, Y. Wang, H.H. Zhang

Modulating work-hardening behaviors and tensile plasticity of in-situ formed ductile dendrite Ti-based bulk metallic glass composites with tailored dendrite composition

Scripta Mater., 146 (2018), pp. 22-26

https://www.sciencedirect.com/science/article/pii/S1359646217306334, Accessed 9th Feb 2020
View PDFView articleGoogle Scholar

[18]

Y. Wu, D. Ma, Q.K. Li, A.D. Stoica, W.L. Song, H. Wang, X.J. Liu, G.M. Stoica, G.Y. Wang, K. An, X.L. Wang, M. Li, Z.P. Lu

Transformation-induced plasticity in bulk metallic glass composites evidenced by in-situ neutron diffraction

Acta Mater., 124 (2017), pp. 478-488, 10.1016/j.actamat.2016.11.029
View PDFView articleView in ScopusGoogle Scholar

[19]

L. Zhang, R.L. Narayan, H.M. Fu, U. Ramamurty, W.R. Li, Y.D. Li, H.F. Zhang

Tuning the microstructure and metastability of β-Ti for simultaneous enhancement of strength and ductility of Ti-based bulk metallic glass composites

Acta Mater., 168 (2019), pp. 24-36, 10.1016/j.actamat.2019.02.002
View PDFView articleView in ScopusGoogle Scholar

[20]

D.C. Hofmann

Shape memory bulk metallic glass composites

Science, 329 (2010), pp. 1294-1295, 10.1126/science.1193522
View in ScopusGoogle Scholar

[21]

F. Szuecs, C.P.P. Kim, W.L.L. Johnson, F. Szuecst

Mechanical properties of Zr56.2Ti13.8Nb5.0Cu6.9Ni5.6Be12.5 ductile phase reinforced bulk metallic glass composite

Acta Mater., 49 (2001), pp. 1507-1513, 10.1016/S1359-6454(01)00068-4
View PDFView articleView in ScopusGoogle Scholar

[22]

S. González, P. Pérez, E. Rossinyol, al, T. Brink, K. Albe, A. Zaheri, F. Abdeljawad, M. Haataja

Simulation study of mechanical properties of bulk metallic glass systems: martensitic inclusions and twinned precipitates Related content Drastic influence of minor Fe or Co additions on the glass forming ability, martensitic transformations and mechanical properties of shape memory Zr-Cu-Al bulk metallic glass composites Simulation study of mechanical properties of bulk metallic glass systems: martensitic inclusions and twinned precipitates

Model. Simul. Mater. Sci. Eng. Model. Simul. Mater. Sci. Eng., 22 (2014), p. 17, 10.1088/0965-0393/22/8/085008
View in ScopusGoogle Scholar

[23]

(n.d.)

M.R.-J. of E. and A. Sciences, undefined

Modelling and Simulation of Solidification Phenomena during Additive Manufacturing of Bulk Metallic Glass Matrix Composites (BMGMC)—A Brief Review

Scirp.Org (2018)

https://www.scirp.org/journal/paperinformation.aspx?paperid=85500, Accessed 5th Mar 2021
Google Scholar

[24]

M.K. Shete, I. Singh, R. Narasimhan, U. Ramamurty

Effect of strain hardening and volume fraction of crystalline phase on strength and ductility of bulk metallic glass composites

Scripta Mater., 124 (2016), pp. 51-55, 10.1016/j.scriptamat.2016.06.020
View PDFView articleView in ScopusGoogle Scholar

[25]

M.K. Shete, T. Dutta, I. Singh, R. Narasimhan, U. Ramamurty

Tensile stress-strain response of metallic glass matrix composites reinforced with crystalline dendrites: role of dendrite morphology

Intermetallics, 83 (2017), pp. 70-82, 10.1016/j.intermet.2016.12.006
View PDFView articleView in ScopusGoogle Scholar

[26]

(n.d.)

T. Dutta

R.N.-E.F. Mechanics, Undefined 2020, Numerical Study of Stationary Cracks in Bulk Metallic Glass Composites under Mode I, Small Scale Yielding Conditions

Elsevier

https://www.sciencedirect.com/science/article/pii/S0013794420308936?casa_token=Se4ZLthrRV0AAAAA:7Yz98IK_UbhplsZXpnFLqTB0V4lUbI2gTp85w_3ZnQxic8uF01A2ztUvUMcFshYXhkXvaGQZHZU, Accessed 5th Mar 2021
Google Scholar

[27]

T. Dutta, A. Chauniyal, I. Singh, R. Narasimhan

Numerical investigation of tensile response of notched bulk metallic glass composite specimens

Model. Simulat. Mater. Sci. Eng., 28 (2020), Article 085002, 10.1088/1361-651X/abb98f
View in ScopusGoogle Scholar

[28]

ASTM E8/E8M - 11

Standard test methods for tension testing of metallic materials

https://doi.org/10.1520/E0008 (2011)
Google Scholar

[29]

M.-S. Ding, L. Tian, W.-Z. Han, J. Li, E. Ma, Z.-W. Shan

Nanobubble fragmentation and bubble-free-channel shear localization in helium-irradiated submicron-sized copper

Phys. Rev. Lett., 117 (2016), p. 215501, 10.1103/PhysRevLett.117.215501
View in ScopusGoogle Scholar

[30]

R.L. Narayan, L. Tian, D. Zhang, M. Dao, Z.W. Shan, K.J. Hsia

Effects of notches on the deformation behavior of submicron sized metallic glasses: insights from in situ experiments

Acta Mater. (2018), 10.1016/j.actamat.2018.05.041
Google Scholar

[31]

L. Tian, Y.-Q.Q. Cheng, Z.-W.W. Shan, J. Li, C.-C.C. Wang, X.-D.D. Han, J. Sun, E. Ma

Approaching the ideal elastic limit of metallic glasses

https://doi.org/10.1038/ncomms1619 (2012)
Google Scholar

[32]

R.L. Narayan, L. Tian, D. Zhang, M. Dao, Z.W. Shan, K.J. Hsia

Effects of notches on the deformation behavior of submicron sized metallic glasses: insights from in situ experiments

Acta Mater., 154 (2018), pp. 172-181, 10.1016/j.actamat.2018.05.041
View PDFView articleView in ScopusGoogle Scholar

[33]

S.B. Maisel, W.S. Ko, J.L. Zhang, B. Grabowski, J. Neugebauer

Thermomechanical response of NiTi shape-memory nanoprecipitates in TiV alloys

Phys. Rev. Mater. (2017), 10.1103/PhysRevMaterials.1.033610
Google Scholar

[34]

W. Duan, X. Liang, X. Yang, Y. Wang, B. Luan

Lattice stability and elastic properties of Zr-Ti-X alloys (X = Al, V) by the first principles study

Metals, 10 (2020), p. 1317, 10.3390/met10101317
Google Scholar

[35]

S. Plimpton

Fast parallel algorithms for short-range molecular dynamics

J. Comput. Phys. (1995), 10.1006/jcph.1995.1039
Google Scholar

[36]

A. Stukowski, V.V. Bulatov, A. Arsenlis

Automated identification and indexing of dislocations in crystal interfaces

Model. Simulat. Mater. Sci. Eng. (2012), 10.1088/0965-0393/20/8/085007
Google Scholar

[37]

J. Booth, J. Lewandowski, J. Carter

EBSD analysis for microstructure characterization of Zr-based bulk metallic glass composites

Microsc. Microanal, Cambridge University Press (2014), pp. 852-853, 10.1017/S1431927614005984
View in ScopusGoogle Scholar

[38]

M. Niinomi

Mechanical properties of biomedical titanium alloys

Mater. Sci. Eng., 243 (1998), pp. 231-236, 10.1016/s0921-5093(97)00806-x
View PDFView articleView in ScopusGoogle Scholar

[39]

D. Kiener, W. Grosinger, G. Dehm, R. Pippan

A further step towards an understanding of size-dependent crystal plasticity: in situ tension experiments of miniaturized single-crystal copper samples

Acta Mater., 56 (2008), pp. 580-592, 10.1016/j.actamat.2007.10.015
View PDFView articleView in ScopusGoogle Scholar

[40]

D. Kang, D.C. Baars, A. Mapar, T.R. Bieler

STUDY OF SLIP AND DEFORMATION IN HIGH PURITY SINGLE CRYSTAL NB FOR ACCELERATOR CAVITIES*

(2015)

Google Scholar

[41]

J.W. Qiao, S. Wang, Y. Zhang, P.K. Liaw, G.L. Chen

Large plasticity and tensile necking of Zr-based bulk-metallic-glass-matrix composites synthesized by the Bridgman solidification

Appl. Phys. Lett., 94 (2009), Article 151905, 10.1063/1.3118587
View in ScopusGoogle Scholar

[42]

D. Kiener, A.M. Minor

Source truncation and exhaustion: insights from quantitative in situ TEM tensile testing

Nano Lett., 11 (2011), pp. 3816-3820, 10.1021/nl201890s
Google Scholar

[43]

D. Kiener, A.M. Minor

Source-controlled yield and hardening of Cu(1 0 0) studied by in situ transmission electron microscopy

Acta Mater., 59 (2011), pp. 1328-1337, 10.1016/j.actamat.2010.10.065
View PDFView articleView in ScopusGoogle Scholar

[44]

G. Richter, K. Hillerich, D.S. Gianola, R. Mönig, O. Kraft, C.A. Volkert

Ultrahigh strength single crystalline nanowhiskers grown by physical vapor deposition

Nano Lett., 9 (2009), pp. 3048-3052, 10.1021/nl9015107
View in ScopusGoogle Scholar

[45]

F. Shimizu, S. Ogata, J. Li

Theory of shear banding in metallic glasses and molecular dynamics calculations

https://doi.org/10.2320/matertrans.MJ200769 (2007)
Google Scholar

[46]

F. Shimizu, S. Ogata, J. Li

Yield point of metallic glass

Acta Mater., 54 (2006), pp. 4293-4298, 10.1016/j.actamat.2006.05.024
View PDFView articleView in ScopusGoogle Scholar

[47]

Y. Wang, J. Li, A. V Hamza, T.W. Barbee

Ductile crystalline-amorphous nanolaminates

Proc. Natl. Acad. Sci. U.S.A., 104 (2007), pp. 11155-11160, 10.1073/pnas.0702344104
View in ScopusGoogle Scholar

[48]

J.-Y. Kim, D. Jang, J.R. Greer

Nanolaminates utilizing size-dependent homogeneous plasticity of metallic glasses

Adv. Funct. Mater., 21 (2011), pp. 4550-4554, 10.1002/adfm.201101164
View in ScopusGoogle Scholar

[49]

Y.Q. Wang, K. Wu, J.Y. Zhang, G. Liu, J. Sun

Probing the size- and constituent-mediated mechanical properties and deformation behavior in crystalline/amorphous nanolaminates

Nanoscale, 10 (2018), pp. 21827-21841, 10.1039/c8nr07129b
View in ScopusGoogle Scholar

[50]

Y. Wang, D. Kiener, X. Liang, J. Bian, K. Wu, J. Zhang, G. Liu, J. Sun

Constituent constraining effects on the microstructural evolution, ductility, and fracture mode of crystalline/amorphous nanolaminates

J. Alloys Compd., 768 (2018), pp. 88-96, 10.1016/j.jallcom.2018.07.177
View PDFView articleView in ScopusGoogle Scholar

[51]

L. Zhang, R.L. Narayan, B.A. Sun, T.Y. Yan, U. Ramamurty, J. Eckert, H.F. Zhang

Cooperative shear in bulk metallic glass composites containing metastable β-Ti dendrites

Phys. Rev. Lett. (2020), 10.1103/PhysRevLett.125.055501
Google Scholar

[52]

P.S. Singh, *et al.*
Effect of strain rate and temperature on the plastic deformation behaviour of a bulk metallic glass composite
Mater. Sci. Eng.: A, 534 (2012), pp. 476-484, 10.1016/j.msea.2011.11.096
View PDFView articleView in ScopusGoogle Scholar

[53]

Devashish Rajput, *et al.*
Shear fracture in bulk metallic glass composites
Acta Mater. (2021), Article 116963, 10.1016/j.actamat.2021.116963
In press
https://www.sciencedirect.com/science/article/pii/S1359645421003438
View at publisherGoogle Scholar